A deep-learning and transfer-learning hybrid aerosol retrieval algorithm for FY4-AGRI: Development and verification over Asia

Disong Fu [a], Hongrong Shi [a, b], Christian A. Gueymard [c], Dazhi Yang [d], Yu Zheng [e], Huizheng Che [e, *], Xuehua Fan [a], Xinlei Han [f, g], Lin Gao [h], Jianchun Bian [a, i], Minzheng Duan [a, i], Xiangao Xia [a, i, **]

[a] Key Laboratory of Middle Atmosphere and Global Environment Observation, Institute of Atmospheric Physics, Chinese Academy of Sciences, Beijing 10029, China

[b] Key Laboratory of Cloud-Precipitation Physics and Severe Storms, Institute of Atmospheric Physics, Chinese Academy of Sciences, Beijing 100029, China

[c] Solar Consulting Services, Colebrook, NH 03576, USA

[d] School of Electrical Engineering and Automation, Harbin Institute of Technology, Harbin 150006, China

[e] State Key Laboratory of Severe Weather & Key Laboratory of Atmospheric Chemistry, Institute of Atmospheric Composition and Environmental Meteorology, Chinese Academy of Meteorological Sciences, China Meteorological Administration, Beijing 100081, China

[f] National Institute of Natural Hazards, Ministry of Emergency Management of China, Beijing, 100085, China

[g] Key Laboratory of Compound and Chained Natural Hazards Dynamics, Ministry of Emergency Management of China, Beijing 100085, China

[h] National Satellite Meteorological Center, China Meteorological Administration, Beijing 100081, China

[i] University of Chinese Academy of Sciences, Beijing 100049, China

[*, **] Corresponding author: Huizheng Che, Xiangao Xia

Email: chehz@cma.gov.cn, xxa@mail.iap.ac.cn

ABSTRACT:

The Advanced Geosynchronous Radiation Imager (AGRI) is a mission-critical instrument for the Fengyun series of satellites. AGRI acquires full-disk images every 15 min and views East Asia every 5 min through 14 spectral bands, enabling the detection of highly variable aerosol optical depth (AOD). Quantitative retrieval of AOD has hitherto been challenging, especially over land. In this study, an AOD retrieval algorithm is proposed to combine deep learning and transfer learning. The algorithm uses core concepts from both the Dark Target (DT) and Deep Blue (DB) algorithms to select features for the machine-learning algorithm, allowing for AOD retrieval at 550 nm over both dark and bright surfaces. The algorithm consists of two steps: (1) a baseline deep neural network (DNN) with skip connections is developed using 10-min Advanced Himawari Imager AODs as the target variable, and (2) sunphotometer AODs from 89 ground-based stations are used to fine-tune the DNN parameters. Out-of-station validation shows that the retrieved AOD has attained a high accuracy, characterized by a coefficient of determination (R^2) of 0.70, a mean bias error (MBE) of 0.03, and a percentage of data within the expected error (EE) of 70.7%. A sensitivity study reveals that the top-of-atmosphere reflectance at 650 and 470 nm, as well as the surface reflectance at 650 nm, are the two largest sources of uncertainty that impact the retrieval. In a case study of monitoring an extreme aerosol event, the AGRI AOD is found able to capture the detailed temporal evolution of the event. This work demonstrates the superiority of the transfer learning technique in satellite AOD retrievals and the applicability of the retrieved AGRI AOD in monitoring extreme pollution events.

Keywords: Aerosol optical depth; Retrieval algorithm; Deep learning; Transfer learning; AGRI

1. Introduction

Detailed information on aerosols is essential for a broad range of geoscience domains, such as the Earth's radiation balance [1], climate change [2], air quality [3], and human health [4], just to name a few. Aerosol optical depth (AOD), defined as the vertical integral of the extinction coefficient of atmospheric aerosols from the ground to the top of the atmosphere (TOA), is a widely used and most important optical parameter to characterize atmospheric aerosols.

In parallel, ground-based sunphotometer remote sensing is widely regarded as the most accurate method for obtaining AOD. Sunphotometer AODs are thus often used as ground truth to validate a wide variety of aerosol products from satellite remote sensing, chemical transport models (CTM), and atmospheric reanalysis [5–9]. The Aerosol Robotic Network (AERONET) has started to be developed more than 25 years ago and has grown to include hundreds of sunphotometric stations worldwide [10,11]. In Asia, there are also a few regional sunphotometer networks, such as the SKYradiometer NETwork (SKYNET) [12]. In China, three independent sunphotometer networks, namely, CARSNET (the Chinese Aerosol Research Network [13]), CSHNET (the Chinese Sun Hazemeter Network, now known as CARE-China [14]), and SONET (the Sun–Sky Radiometer Observation Network [15]), have been established to meet the increasing demand for research-grade aerosol data. In addition, a few stations from the international AERONET and SKYNET networks also operate throughout China. All these networks play a vital role in characterizing aerosol properties over China. However, the high spatiotemporal variability of aerosols cannot be fully captured by these sparsely distributed sunphotometer instruments. Hence, satellite remote sensing is highly needed to provide AOD products with high spatiotemporal coverage.

Satellite remote sensing, which mainly refers to the sensing provided by polar-orbiting and geostationary satellites, has been ubiquitously used to acquire aerosol properties spatiotemporally. Polar orbiting satellites can detect global AOD but have relatively long revisit periods. In comparison, geostationary satellites have the advantage of providing high-frequency aerosol observations (~5–15 min) at good spatial resolutions. The current sensors of that kind include the Spinning Enhanced Visible and Infrared Imager (SEVIRI) onboard Meteosat Second Generation (MSG) from the European Organization for the Exploitation of Meteorological Satellites (EUMETSAT) [16], the Advanced Baseline Imager (ABI) of Geostationary Operational Environmental Satellites (GOES)-16/17 from the National Oceanic and Atmospheric Administration (NOAA), the Advanced Himawari Imager (AHI) onboard Himawari-8 and its successor[1], Himawari-9, from the Japan Meteorological Agency (JMA) [17], and the Geostationary Ocean Color Imager II (GOCI-II) of the Geostationary Korea Multi-Purpose Satellite 2B (GEO-KOMPSAT-2B) [18]. Fig. 1 presents the positions and coverages of the six geostationary satellites that cover China wholly or

---

[1] Himawari-9 became JMA's operational satellite on December 13, 2022; it replaced Himawari-8, which was then placed in stand-by mode.

partially, namely, Meteosat-9 (also known as the Indian Ocean Data Coverage, IODC) at 45.5°E, Himawari-8/9 at 140.7°E, GEO-KOMPSAT-2B at 128°E, FY-4A (Fengyun-4A) at 104.7°E, and FY-4B (Fengyun-4B) at 133°E. Although Himawari-8/9 and IODC cover parts of China, none of these satellites can provide data for the entire country with a good field of view. In contrast, FY-4A and FY-4B can now provide full coverage and high-frequency measurements over China and neighboring countries [19]. They respectively constitute the first and second instance of the new generation of Chinese geostationary meteorological satellites. Both satellites carry various instruments, including the Advanced Geostationary Radiation Imager (AGRI) sensor , which is central to the present study and whose capabilities have been reviewed by Zhang et al. [20].
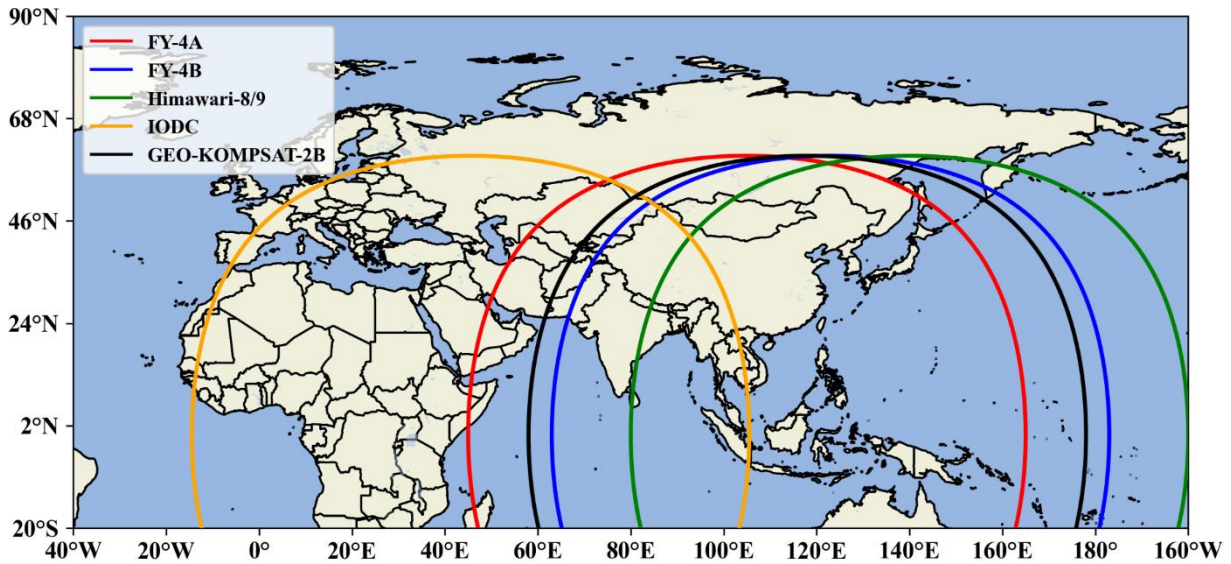
Fig. 1. Observation areas of the six geostationary satellites over the Eastern Hemisphere. Note: Himawari-8 and -9 have the same footprint.

The most challenging task in passive satellite AOD retrieval over land is to separate the surface and aerosol contributions to the reflected radiance that is sensed by spaceborne radiometers. This is especially true when the surface is highly reflective (e.g., snow or bright sand) and the AOD signal is low. Researchers have developed various physical schemes to address this problem, which can be divided into four main categories: (1) establishment of surface reflectance relationships between the visible and other bands, such as the Dark Target (DT) method [21]; (2) construction of pre-calculated static surface reflectance database, with the Deep Blue (DB) and the

enhanced Deep Blue algorithm [22–24] as typical examples; (3) use of a multi-angle method, as represented by the multi-angle implementation of atmospheric correction (MAIAC) [25]; (4) use of polarization information, such as the usage of the Generalized Retrieval of Aerosol and Surface Properties (GRASP) unified algorithm in Polarization and Directionality of the Earth's Reflectances (POLDER, [26]). There are also already some attempts that use the above algorithms for AOD retrieval from geostationary satellites. For instance, the NOAA GOES-16 ABI AOD over land uses a DT-based method [27]. In contrast, the operational AHI land aerosol product, released by the Japan Aerospace Exploration Agency (JAXA), uses a DB-type method, where the second lowest reflectance measurement in a month is atmospherically corrected to represent the surface reflectance [28].

Benefiting from the advancement of computer technology, machine learning (ML) has rapidly gained great interest within the remote-sensing field. Most critically, ML can help model the complex relationship between satellite-observed TOA reflectance and surface-based AOD. She et al. [29] utilized a deep neural network (DNN) model to estimate AOD from AHI, with AOD data from 76 AERONET sites serving as the ground truth. The root mean-squared error (RMSE) achieved by their model was 0.17, demonstrating its effectiveness in AOD estimation. In a similar way, Yeom et al. [30] also employed DNN, but focused on the GOCI sensor and AERONET AOD data over Northeast Asia. Their validation results exhibited high accuracy for the DNN-generated AOD when compared to either traditional support vector regression (SVR) or random forest (RF) models. In contrast to previous works, Kang et al. [31] introduced channel difference features into the DNN model, indirectly incorporating surface reflectance information. The coefficient of determination (R^2) of 10-fold cross-validation reached 0.93 and 0.92 for Light Gradient Boosting Machine (LightGBM) and RF, respectively. Chen et al. [32] directly utilized surface reflectance data derived from the Moderate Resolution Imaging Spectroradiometer (MODIS) alongside ground-measured AOD to train a Convolutional Neural Network (CNN) model. The evaluation demonstrated that ≈68% of the AOD values fell within the expected error (EE) range of $\pm$ (0.05 + 15%). It is emphasized that even though these studies employed different sensors, methods, and input features, they all relied solely upon the ground observations, which are being sampled very sparsely with respect to the area over which the retrieval is required.

Whereas the above-mentioned literature leverages the observations from AHI, GOCI, and

MODIS, there is no operational AOD product from AGRI yet, although some attempts have been made. For instance, Jiang et al. [33] developed an algorithm for retrieving AGRI AOD over land. This algorithm uses a monthly surface reflectance band-ratio database and look-up tables (LUT) computed by the Second Simulation of a Satellite Signal in the Solar Spectrum Vector (6SV) model to retrieve hourly AOD. The accuracy was reported to be fairly high, with an R^2 of 0.71, RMSE of 0.16, and ~60% of the retrieved AODs within EE. Xie et al. [34] developed a multi-channel (MC) algorithm for AGRI over South Asia. This algorithm assumes that the relationships between the surface reflectance in different bands remain stable over a period of two weeks. The surface reflectance is derived when aerosol loading is low and MODIS AOD is used for atmospheric correction. The MC algorithm is claimed to be applicable to both dark targets and bright surfaces. In comparison to AERONET AODs, the MC-retrieved AGRI AOD shows high accuracy, with RMSE and EE of the data being 0.16 and 63.71%, respectively. Ding et al. [35] recently applied the so-called Neural Network AEROsol Retrieval for Geostationary Satellite (NNAeroG) to the full-disk area of AGRI. The AOD data from 111 sunphotometer sites (AERONET + SONET) were used to train the network, and 28 other sites were reserved for independent validation. The AGRI AOD predicted by NNAeroG was found to be consistent with the sunphotometer AOD data (RMSE = 0.24, R^2 = 0.73, EE = 58.7%).

To summarize the advances in satellite AOD retrieval, the physical retrieval methods (such as DT or DB) usually require prior knowledge of aerosol properties, except for the unknown AOD over the area of interest. A radiative transfer model is run to build a LUT for the subsequent AOD retrieval. However, the size of LUT grows exponentially with predefined parameters and the LUT is usually unique for each sensor. This means that the physical retrieval method is difficult to adapt to new contexts. In addition, the rapid development in installed sunphotometer stations is not fully exploited by physical retrieval methods, because these stations are used only to characterize aerosol properties or as verification references. In connection with the abovementioned ML-based AOD algorithms, only sunphotometer-based AODs have been used as targets so far. One notable pitfall of this approach is that the ground-based stations are still relatively scarce and unevenly distributed, which would inevitably lower the confidence in the AOD retrieval over areas that are not covered by at least a few stations. Considering the high heterogeneity of aerosol and surface properties, it seems very improbable that ML models based on limited training samples can be

6

167 universal.

168   Given these problems, the goal of this contribution is to develop a novel AGRI AOD retrieval
169 algorithm using both deep-learning and transfer-learning techniques. The innovation here includes
170 the following three aspects. First, the features of the machine-learning model are selected based
171 on the core physical concepts of the DT and DB algorithms. Second, a transfer-learning technique
172 is used to overcome the limitation of training samples. This involves training a model by using
173 the AHI AOD as a target whose parameters are tuned by using as many sunphotometer measure-
174 ments as possible. Since AHI AODs are used in that process, this algorithm enables the synergy
175 between physical retrieval algorithm and machine-learning method. Finally, a detailed sensitivity
176 analysis is performed to discuss the potential sources of error.

177

2. Data and methods

178

2.1 AGRI sensor

180   FY-4A was launched on December 11, 2016, and remains positioned at a longitude of 104.7ºE.
181 It is the first of China's latest-generation geostationary meteorological satellites [19,36]. Com-
182 pared to the instruments that equipped the first generation of Chinese geostationary satellites (FY-
183 2), the AGRI onboard FY-4A has significant improvements in several aspects. First, the number
184 of spectral bands increases from 5 to 14, providing more refined spectral information. Second, the
185 snapshot interval for the full-disk Earth-view images is reduced from 30 to 15 min, while the
186 central and eastern Asia regions are observed every 5 min. This high temporal resolution can help
187 capture high-frequency variations in the observed processes. Third, AGRI has a higher spatial
188 resolution: 1 km in the visible, 2 km in the near-infrared, and 4 km in the other IR spectral bands.
189 This facilitates the analysis of small-scale spatial variations, which is vital to the understanding of
190 the local aerosols' characteristics and transport mechanism.

191   For this study, a subset of the AGRI/FY-4A Level-1 (L1) 4-km dataset with 5-min temporal
192 resolution was obtained from http://data.nsmc.org.cn, spanning the full year of 2018. The cosines
193 of the satellite view zenith angle and solar zenith angle (CSVA and CSZA), seven bands of AGRI
194 (470, 650, 825, 1375, 1610, 2250 nm, and 10.7 μm), as well as a few quantities obtained by com-
195 bining different bands, are taken as features during the ML model development (see Section 3 for

details).

2.2 AHI AOD from Himawari-8

The AHI radiometer on Himawari-8/9 is equipped with 16 channels, with a spatial resolution of 0.5–2 km and a temporal resolution of 10 min [17]. An optimal estimation algorithm was developed to simultaneously retrieve AOD, single scattering albedo (SSA) at 500 nm, and Ångström exponent (AE) at 400–600 nm [28]. Over land, the algorithm assumes that the surface reflectance remains unchanged in a month; the second minimum reflectance on an hourly scale is selected to establish the surface reflectance database. Over oceans, the sea surface reflectance is calculated based on the Cox and Munk method [37]. In this study, the Version 3 Level-2 AOD retrievals with either "very good" or "good" quality at 10-min resolution are used to train a baseline model (see Section 3 for details). Eq. (1) is used to obtain AOD at 550 nm using AHI's AE and AOD at 500 nm:

$$\tau_{550} = \tau_{500} \times (550/500)^{-\mathrm{AE}}. \tag{1}$$

where τ_{550} and τ_{500} are the AODs at 550 and 500 nm, respectively.
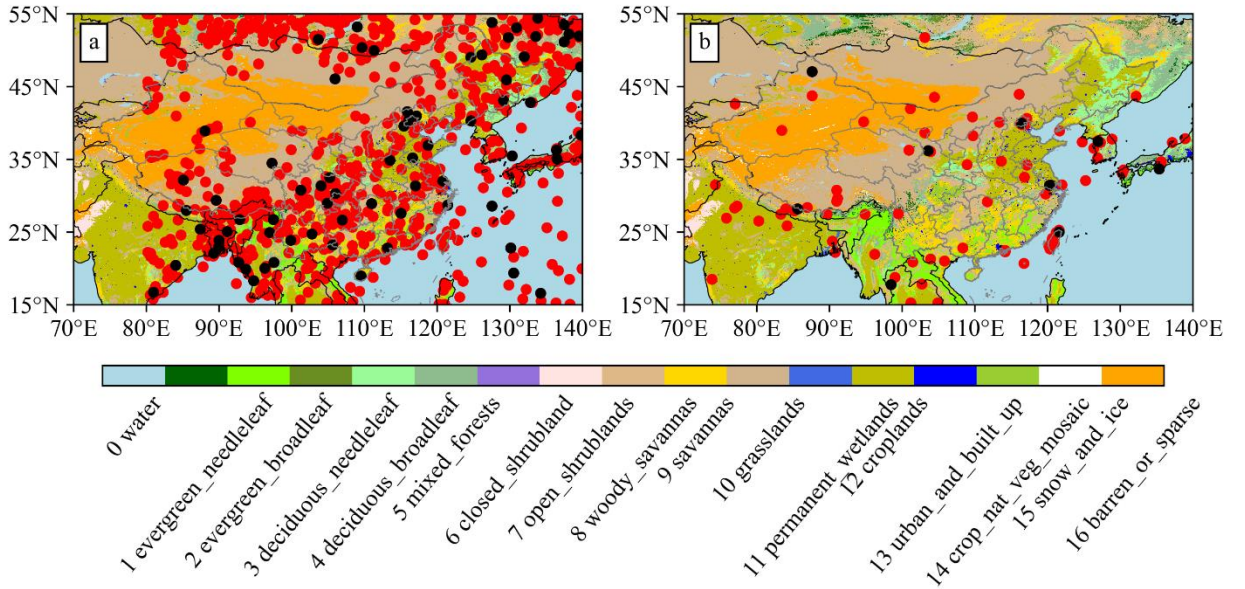
Fig. 2. Spatial distribution of (a) the 900 sampling locations used for the baseline model development, and (b) the 89 sunphotometer stations used for fine-tuning in this study. The 900 sampling locations are nearly uniformly selected in the Himawari-8 domain area according to the MCD12C1 land-cover types. Sites marked with red and black colors indicate the training and

testing sites used in the model, respectively. The background layer shows the MCD12C1 land-cover types.

2.3 Sunphotometer AOD

In the transfer learning, ground-based sunphotometer aerosol products are used as a reference to fine-tune the baseline model. Both AERONET and CARSNET AOD products are used here. CARSNET is a ground-based aerosol monitoring system established by the China Meteorological Administration (CMA). CARSNET sunphotometers are calibrated annually according to a stringent calibration protocol, resulting in AOD measurements with the same accuracy as those from AERONET [13]. AOD data at 89 stations over Asia (CARSNET + AERONET) are used in this study (Fig. 2). To the best of the authors' knowledge, this is by far the largest number of stations with sunphotometer data ever reported in the literature for that part of Asia. The AOD at 550 nm is simply interpolated from its counterparts at 440, 675, 870, and 1020 nm, using the interpolation method described in [9].

2.4 Auxiliary data

The auxiliary data include hourly meteorological quantities derived from the ERA5 reanalysis [38] produced by the European Centre for Medium-Range Weather Forecasts (ECMWF) at a spatial resolution of $0.25° \times 0.25°$. These quantities are: 2-meter temperature (T2M, K), total column water vapor (PWV, kg m^{-2}), total columnar ozone (O3, kg m^{-2}), boundary layer height (BLH, m), and surface pressure (SP, Pa). Elevation (ELV, m) from the shuttle radar topography mission digital elevation model (SRTMDEM) with a 90-m spatial resolution is used as a predictor to explain the AOD's elevation dependence. A coarse time variable (Time), namely the day of year, is used to reflect the seasonality of AOD; it is encoded as $\cos(2\pi \times \text{Time}/365)$. Finally, since previous studies have shown that the satellite-derived AOD uncertainty varies with surface types [39], the land cover types obtained from the MODIS Land Cover Climate Modeling Grid (MCD12C1) Version-6 data product [40] are also used as a feature.

3. Retrieval methodology

The uncertainty in satellite aerosol retrievals comes from four major sources: sensor calibration, cloud detection, aerosol model selection, and surface reflectance determination [41,42]. Here, much attention is given to cloud detection, surface reflectance estimation, and aerosol retrieval strategy. AGRI's calibration accuracy is 5% for reflective solar bands [19], which will be discussed in subsection 4.4, along with the sensitivity analysis.

3.1 Cloud/snow/ice/water pixel mask

For the following aerosol retrievals, a simple but robust cloud detection algorithm is firstly developed with reference to Su et al. [42] and the GOES-R ABI Algorithm Theoretical Basis Document [27]. The detection algorithm consists of a set of thresholds and tests, including a reflectance and brightness temperature threshold test, a brightness temperature difference and spatial inhomogeneity test, and a water and snow/ice pixel identification (Table 1).

Table 1. Criteria for the cloud/snow/ice/water pixel masks in this study (R and BT with numerical subscripts represent the TOA reflectance and brightness temperature at the specified wavelengths).

Classes	Criteria
Over land	
Dense cloud	TOA reflectance at 470 nm (R_{470}) > 0.3
Cloud	Brightness temperature at 10.7 μm ($BT_{10.7}$) < 260 K
Edges of cloud	Standard deviation calculated from 3 × 3 pixels at R_{470} > 0.02 and Standard deviation calculated from 3 × 3 pixels at $BT_{10.7}$ > 4.5
Cirrus cloud	Brightness temperature difference at 8.5 μm and 10.7 μm ($BT_{8.5} - BT_{10.7}$) > 1.0 or TOA reflectance at 1375 nm (R_{1375}) > 0.018
Water	Normalized difference water index (NDWI)[†] > 0.2
Snow	Normalized difference snow/ice index (NDSI)[§] > 0.3 and not water or cloud
Over ocean	
Dense cloud	TOA reflectance at.860 nm (R_{860}) > 0.3
Cirrus cloud	TOA reflectance at 1375 nm (R_{1375}) > 0.018
Edges of cloud	Standard deviation calculated from 3 × 3 pixels at R_{2250} > 0.008
Ice	NDSI > 0.3 and R_{640} > 0.2 and R_{870} > 0.17 and $BT_{10.7}$ < 275K

[†] NDWI is defined as the difference between TOA reflectance at 510 nm and 860 nm ($R_{650} - R_{825}$) normalized by the sum of these two bands ($R_{650} + R_{825}$).

[§] NDSI is defined as the difference between TOA reflectance at 825 nm and 1600 nm ($R_{825} - R_{1610}$) normalized by the sum of these two bands ($R_{825} + R_{1610}$) [23].

265

*3.2 Estimation of surface reflectance proxy*

Precise discrimination between surface reflectance and aerosol backscattering is critical for accurate AOD retrieval, and was often not carefully considered in previous ML-based algorithms [29,30,43]. To address this potential problem, this study adopts the DB method to create a dynamic hourly surface reflectance database at 470, 650, and 2250 nm for each month. All AGRI measurements that are free of both clouds and snow/ice are retained. Considering that, every three hours, AGRI makes two full disk scans during the first 30 minutes and six regional scans every 5-min for the remaining 30 minutes, there are at least 168 regional scans per month for a single hour. Because satellite reflectance measurements are dominated by the surface reflectance when aerosol loading is low, and because aerosols generally enhance the reflectance measurement, the second lowest hourly TOA reflectance for each pixel in a month is selected here to represent the hourly surface reflectance. It is emphasized that the bidirectional property of surface reflectance is taken into account. As an example, the top and bottom panels of Fig. 3 show the baseline reflectance library at 470, 650, and 2250 nm (ρ_{470}, ρ_{650}, and ρ_{2250}) in May and October, respectively. Note that missing values in some grids are filled using nearest-neighbor interpolation. The spatial distribution of surface reflectance is consistent across the three bands, with the lower values found in southern China and the higher values in the north, west, and northwest of the domain. Based on the two exemplary months shown, seasonal variations in surface reflectance are also evident. These results suggest that the second lowest hourly TOA reflectance can effectively be considered as a proxy for surface reflectance, considering that no atmospheric correction can be applied at that stage. Atmospheric correction requires accurate AOD (generally not available) as well as radiative transfer model simulations [34,44], which would considerably increase the method's complexity. Using the second lowest hourly TOA reflectance simplifies the algorithm because no external data is required.

290

291
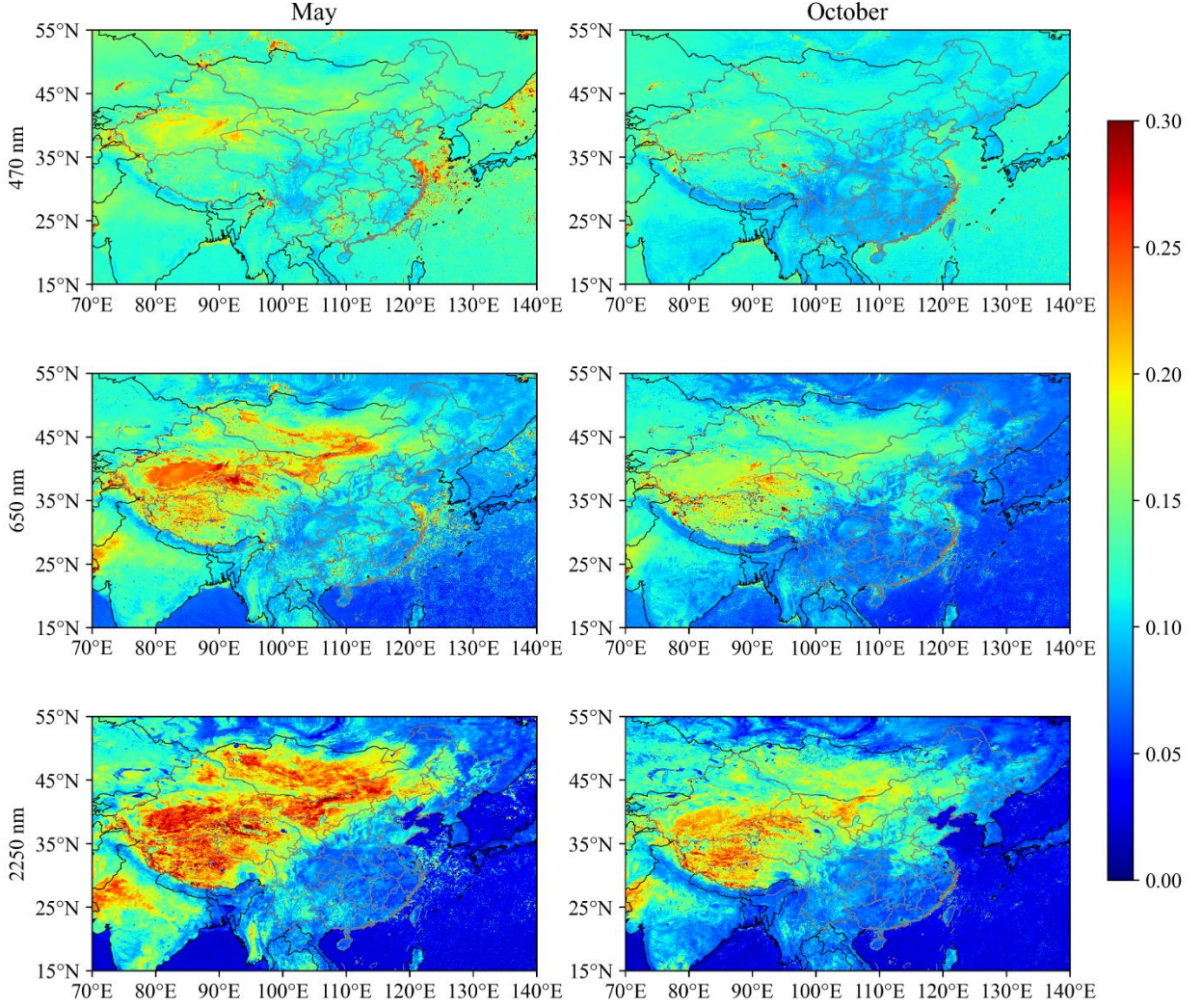
Fig. 3. Surface reflectance at 05:00 UTC in May (left) and October (right) at 470, 650, and 2250 nm (ρ_{470}, ρ_{650}, and ρ_{2250}).

3.3 Machine-learning AOD retrieval model development

Fig. 4 illustrates the overall framework of the retrieval algorithm, which consists of three sub-modules: (i) data preprocessing (orange box); (ii) baseline model tasks (green box); and (iii) trans-fer-learning tasks (blue box). The data stream from multiple sources with different spatiotemporal resolutions is processed into a unified resolution of 4 km. Then, a baseline model (DNN with skip connections) is developed for the initial AOD estimation by using the AHI AOD as target. Finally, the baseline model is improved by the transfer-learning scheme using the sunphotometer AOD as target. The whole procedure can thus be summarized as "preprocessing + DNN + fine-tuning".

305
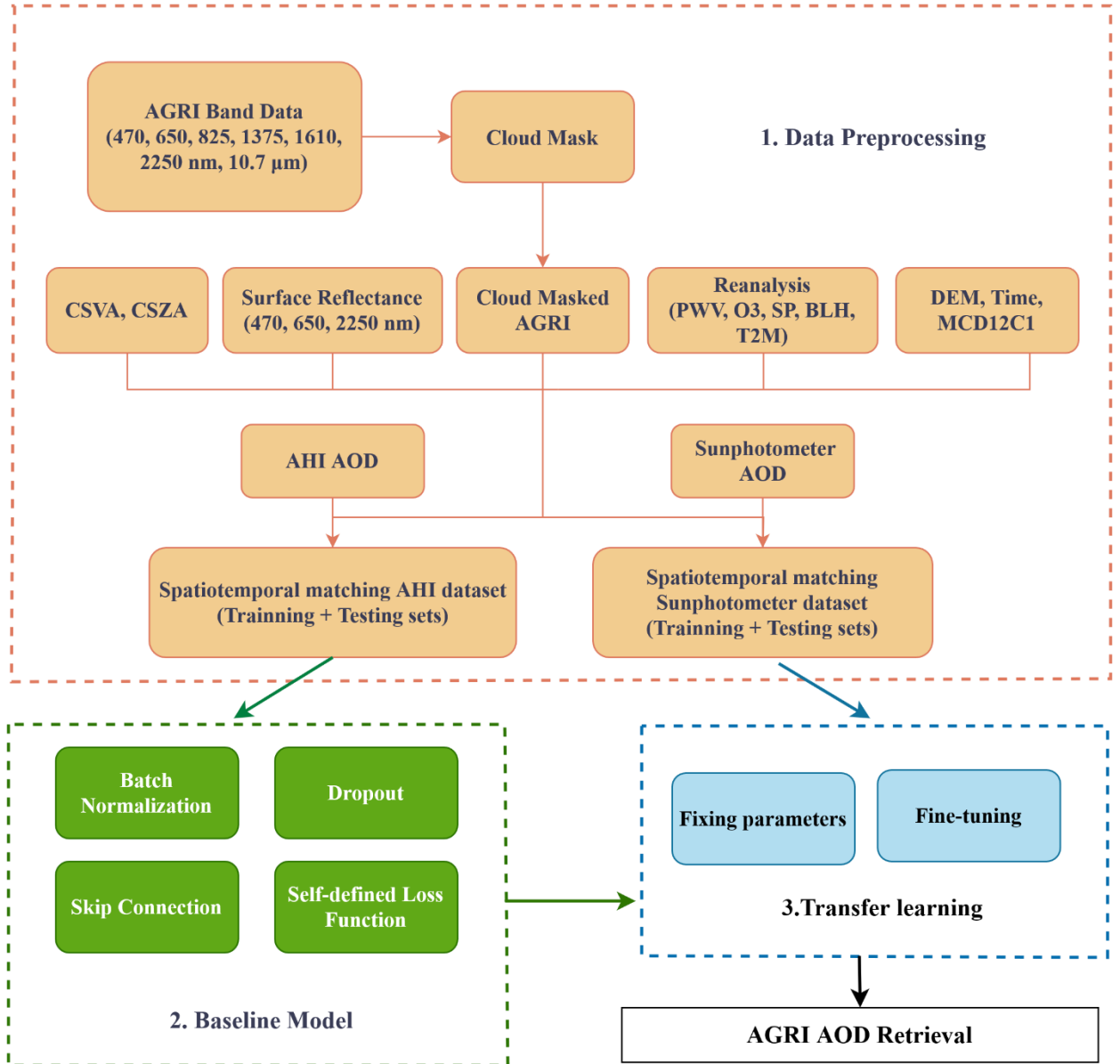
Fig. 4. Flowchart of the deep-learning and transfer-learning hybrid method for AGRI AOD retrievals.

306

307

308

309

3.3.1   Data preprocessing

310

The temporal and spatial resolutions of the original sources are summarized in Table 2. The spatial resolution of all datasets is re-gridded to 4 km by linear interpolation. The variables of the ERA5 reanalysis are assumed to remain constant within each hour. Thus, the ERA5 outputs closest to the AGRI observation time are used as the auxiliary variables. For hybrid deep learning and transfer learning, two models need to be trained sequentially. Thus, the input data in Table 2 needs

311

312

313

314

315

to be matched with both the AHI AOD and sunphotometer AOD, respectively, although the two sets of training-target locations need not coincide. For the AHI AOD, 900 sampling points are nearly uniformly selected from the Himawari-8 domain according to the MCD12C1 land types (i.e., ~60 points for each land type). The AHI AOD over these 900 sampling points for each observation in 2018 is extracted as the target for the training of the baseline model. The input datasets within ±2.5 min of the AHI observation time over these points are also extracted to match the AHI AOD L2 products. The matching of the sunphotometer AOD is the same as for the AHI AOD, except for the actual site locations. After data matching, the total number of AHI and sunphotometer AOD samples are 1,156,090 and 127,794, respectively. A standard normalization is applied to the input data, which standardizes the features by subtracting the mean and scaling to unit variance. The logarithmic transformation is applied to the target variable, since it is standard practice to transform the typically lognormal AOD distribution into approximately normal distribution.

Table 2. Summary of input features for the proposed retrieval algorithm.

| Input source	Variables	Spatial resolution	Temporal resolution
FY4A/AGRI	R_{470}, R_{650}, R_{2250}, CSVA, CSZA	4 km	5 min
Reanalysis	T2M, PWV, O3, SP, BLH	0.25°	1 hour
Surface reflectance	ρ_{470}, ρ_{650}, ρ_{2250}	4 km	5 min
Geographic information	ELV	90 m	yearly
Land cover types	MCD12C1	5 km	yearly
Time variable	Time (Day of Year)	4 km	5 min

3.3.2   Baseline model

A schematic diagram of the baseline model architecture is depicted in Fig. 5. The DNN is constructed by extending the "shallow" network (i.e., ANN with input layer, one hidden layer, and output layer) to multiple hidden layers [45]. In this study, a total of 16 predictors are fed into both the input layer (orange part in Fig. 5) and the 550-nm AHI AOD (the red node in the figure) as the output layer, using four hidden layers. (Note that although there are five gray blocks in the figure, the output from a block is a part of the input of the next block.) The batch normalization, the rectified linear unit (ReLU) activation layer, as well as the dropout mechanism, are integrated into the processing cell (green rectangle in Fig. 5), to regularize the network, add nonlinearity, and reduce overfitting, respectively. Additionally, the skip connection (as represented by the red lines

341 in the figure) is adopted to improve the DNN and to prevent the gradient from vanishing [46–48].

342   In parallel, the state-of-the-art practices for DNN training are used here. The mini-batch gra-

343 dient descent search method is used with a batch size of 512 and 60 epochs to ensure a stable and

344 robust solution. The learning rate is initialized as 0.01, and decreases to 0.001 and 0.0001 at the

345 20 and 40 epochs, respectively. The Adam optimizer is selected because it can converge quickly

346 and stably [49]. Although the target variable (i.e., AOD) is logarithmic, it is still an imbalanced

347 dataset characterized by a long tail to very large values. Studies have indicated that the mean-

348 squared error (MSE) loss would underestimate the most infrequent data points win imbalanced

349 regression problems [50,51]. Therefore, a special loss function is designed to compensate for the

350 underestimation of large AODs:

351

352
$$loss_n = \begin{cases} 0.5 \cdot (y_n - \hat{y}_n)^2, if\ y_n - \hat{y}_n < 0 \\ (y_n - \hat{y}_n)^2,\ otherwise. \end{cases} \tag{2}$$

353

354 If the prediction value $\hat{y}_n$ is larger than the target value y_n, the loss is equal to half of the MSE.

355 Otherwise, the loss is exactly equal to the MSE.

356
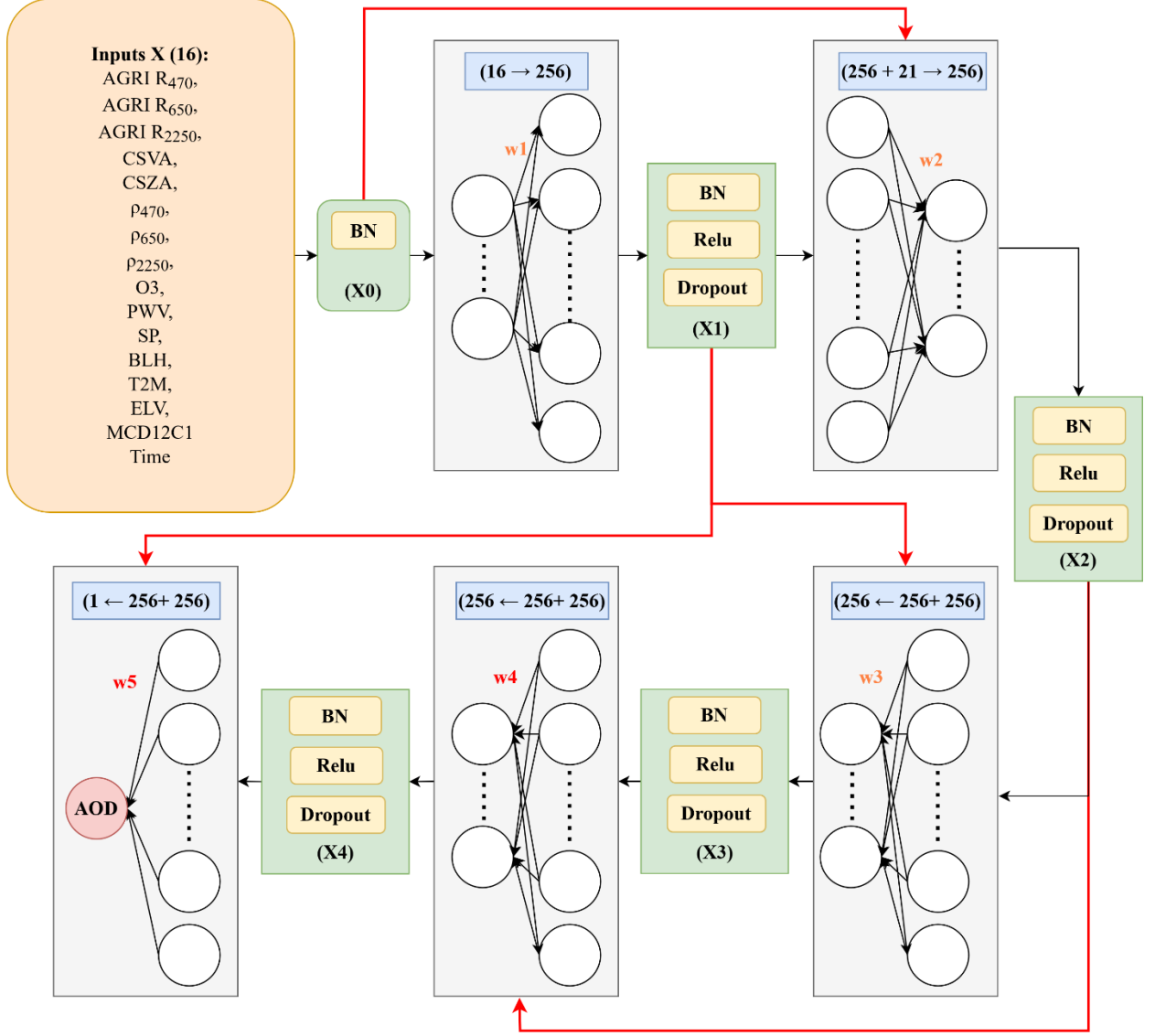
Fig. 5. Architecture of the hybrid model for advanced aerosol retrievals. The circles represent the input and output parameters of one layer. The red lines represent the skip connections. Coefficients w_i (i=1, 2, …, 5) are the weight parameters of the neural network. The numbers in the blue boxes are the input and output dimensions of the network. BN stands for batch normalization.

3.3.3 Transfer learning

Even if the DNN model can accurately reproduce the AHI AOD at 550 nm, the prediction still has a certain degree of uncertainty as compared to ground-based sunphotometer products. This is to be expected because the AHI 550-nm AOD uncertainty is not negligible [52,53]. To further improve prediction accuracy, an additional step of transfer learning is employed.

Transfer learning is a powerful technique that has been used to achieve state-of-the-art results

in many domains [54]. For example, Liu et al. [55] transferred a precipitation fusion model from the source domain to the target domain. As a result, the RMSE and MAE of the precipitation predictions in the Qinghai-Tibet Plateau were significantly reduced (by 27.6 % and 22.5 %, respectively) after fine-tuning.

Generally, the first layer of the pre-trained network is not particularly related to the target dataset, contrarily to the last layer of the network, which is closely related to the target task. Correspondingly, the features of the first layer are called general features, and those of the last layer are called specific features. Therefore, the fine-tuning strategy usually adjusts the parameters of the last full-connected layers of the pre-trained network. In this study, the parameters in the front layers of the pre-trained model are fixed according to Section 3.3.2. The parameters of the full-connected layers (w_4 and w_5 in Fig. 5) are then adjusted by using the new target, i.e., sunphotometer AOD.

4. Results, verification, and discussion

4.1 Model performance in testing datasets and comparison among different methods

Here, two types of validation are used for both the baseline model development and the transfer-learning fine-tuning. First, according to the spatial distribution of the ground sites, 10% of the sites (90 out of 900 sample points and 9 out of 89 ground sites in Fig. 2, respectively) are evenly selected as the testing datasets (out-of-station validation). A 10-fold cross validation is then used in the training process to learn the optimal hyper-parameters of the DNN. The parameters used to evaluate the model performance are R^2, RMSE, mean bias error (MBE), and EE [56,57].

Fig. 6a shows the performance of the baseline model trained only with AHI AOD at 90 AHI testing points. The results have a slight dispersion, with an R^2 of 0.63 and 59.4% of the predictions within EE. The slope value of the linear regression is 0.82, indicating a slight underestimation, most particularly when aerosol loading is high. When the trained baseline model is directly applied to the 9 testing sunphotometer sites (Fig. 6b), a slight degradation in model performance is observed (MBE increases from –0.01 to 0.06, and only 51.3% of the predictions remain within EE). This suggests that the baseline model still has much room for improvement. Compared to Fig. 6b, Fig. 6c shows substantial improvement in the results of the model after fine-tuning, which suggests

that the transfer-learning method has significantly improved the retrieval performance of the base-line model. Specifically, the fine-tuning approach increases R^2 to 0.70, the slope to 0.91, and decreases RMSE and MBE down to 0.15 and 0.03, respectively. Moreover, 70.7% of the results are now within EE.

Although the fine-tuning process does decrease both bias and random errors, Fig. 6c still displays significant scatter. Whereas this might be considered unavoidable to a large extent because of natural variability in the aerosol field, inadequacies in the retrieval procedure, etc., more scrutiny is warranted to help diagnose other possible sources of scatter. The comparisons in Fig. 6 are made between retrievals that represent an average AOD value over a satellite pixel and a point-source observation at a sunphotometric site located somewhere within that pixel. The implicit assumption here is thus that the ground-truth site is truly representative of the pixel in terms of the aerosol field. This is however not always the case in practice, for instance wherever the ground-truth site is at a widely different elevation than the pixel's mean elevation. This particularly occurs when a ground-truth site is located at the bottom of a valley surrounded by high mountains, or conversely, located on top of an isolated high mountain surrounded by low-elevation terrain. For instance, the latter case occurs here with the Gaolanshan station, a top-of-mountain site at an elevation of 1668 m, i.e., above most of the tropospheric aerosol layer. As a result, the observed reference AOD is much lower than the retrieved pixel's mean. Unfortunately, there is currently no specific criterion to evaluate the inherent heterogeneity of a pixel, or to decide whether a ground-truth station should be excluded for this kind of validation. Arbitrarily removing such stations from the testing pool could lead to a loss of statistical significance, and is therefore not an appropriate solution. Another approach would be to introduce a specific elevation correction to modify the retrieved AOD so that it becomes more directly comparable to the local ground truth. This is the process that was followed in [9], for instance, but it is empirical and might not be ideal in all cases. Hence, this has not been attempted here.

424

425
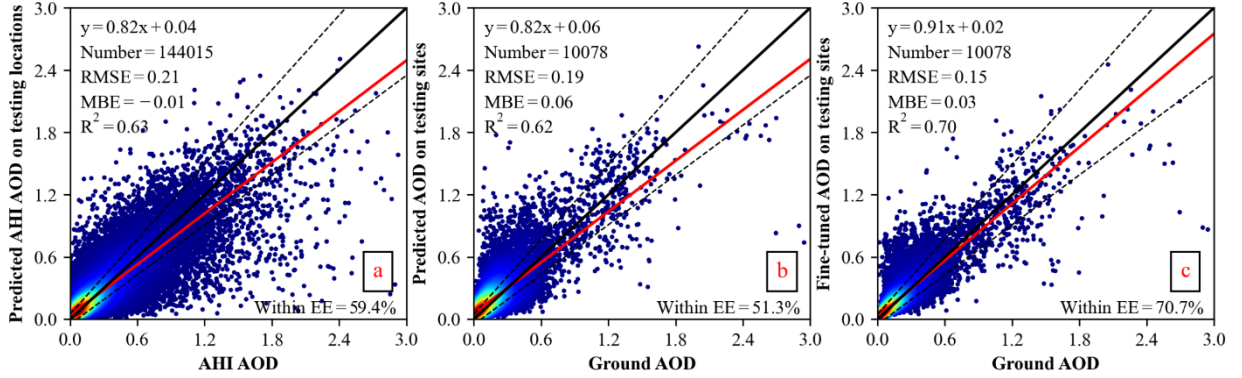
Fig. 6. Performance of the proposed hybrid AOD retrieval algorithm. Performance of (a) baseline model (i.e., DNN with skip connections) at 90 testing AHI locations (b) baseline model at 9 testing sunphotometer sites, and (c) fine-tuned model at 9 testing sunphotometer sites. The solid black lines indicate the 1:1 diagonal. The dashed lines represent the EE envelope.

A comparison of the AGRI AOD retrieval results obtained here with those from previous studies is presented in Table 3. One difficulty is that the comparisons are made against different verification datasets or resolutions, hence the validation results are not directly comparable on a fair basis. The MC method by Xie et al. [34] apparently performs best in terms of RMSE, percentage with EE, and time resolution among the three studies reported here. Nonetheless, the MC method was originally applied over South Asia only, where aerosol properties are not more complex than those over China. Furthermore, the lower-resolution 10-km AOD retrieved by Xie et al. [34] benefits from certain geographical smoothing effects, which tend to make the error smaller. The NNAeroG method by Ding et al. [35] achieves the best R^2, but seems to underestimate at high AODs (slope=0.71, intercept=0.09). This underestimation can be expected since only sunphotometer AODs are used as targets in NNAeroG, and any MSE loss would underestimate the rare occurrences (i.e., very high AODs). In comparison, the lowest RMSE (0.15), highest time/spatial resolution, and largest percentage of data within EE (70.7%) are achieved by the present method. Furthermore, while the present R^2 of 0.70 is slightly lower than the first ranked value of 0.73 obtained by NNAeroG, the method proposed here largely solves the problem of underestimation with self-defined loss function (slope=0.91, intercept=0.02). Overall, Table 3's results suggest that

447 the current algorithm should be able to outperform the other three methods when verified against

448 a same dataset at an identical spatiotemporal resolution.

449

450 **Table 3.** Overview of the performance of AOD retrievals from AGRI in published validation stud-

451 ies. The best value of each metric appears in boldface.

Method and author	Linear equation	RMSE	R^2	Percentage within EE	Time/Spatial resolution	Study area
MC (Xie et al. [34])		0.16	N/A	63.7%	**5 min**/10 km	South Asia (land)
DT-LUT (Jiang et al. [58])		0.31	0.71	60% (EE20)[*]	1 hour/**4 km**	China (land)
NNAeroG (Ding et al. [35])	Y=0.71+0.09	0.24	**0.73**	58.7%	1 hour/**4 km**	Full disk (land)
DNN with transfer learning (this study)	**Y=0.91+0.02**	**0.15**	0.70	**70.7%**	**5 min/4 km**	China (land and ocean)

452 [*] EE20 refers to the expected error envelope of $\pm (0.05 + 20\%)$ used by Jiang et al.

453

454 *4.2 Overview of AOD retrievals*

455 Fig. 7 shows the mean AGRI AOD over the four seasons (MAM, JJA, SON, and DJF). The

456 seasonal mean AGRI AOD values are 0.26, 0.22, 0.16, and 0.21 for them, respectively. High AOD

457 is the norm during MAM and JJA over the Tarim Basin because of the prevalence of desert dust

458 emitted by the Taklamakan Desert during the period [42]. It should be noted that the AHI AOD

459 cannot capture the high AOD over the Tarim Basin because the AHI's observation domain does

460 not cover that region (Fig. 2a). High AOD values also occur over the North China Plain, where

461 the occurrence of haze is typically frequent [59]. The lowest AOD values are observed over the

462 Tibetan Plateau because the high altitude of the Himalaya barrier prevents the aerosol penetration

463 from other regions, e.g., south Asia. The missing values in the north part of the figure for DJF is

464 caused by the ice/snow cover, which prevents meaningful retrievals.

465 Numerous studies have shown that the MAIAC AOD product has high accuracy compared

466 with ground-based sunphotometer AODs [7,60–62]. Therefore, the accuracy statistics between the

467 seasonal mean MAIAC AOD and AGRI AOD in the figure further demonstrate the reliability of

468 the latter, with R^2 ranging from 0.50 to 0.68, maximum MBE less than 0.03 and at least 60.1%

469 data within EE.

470

471
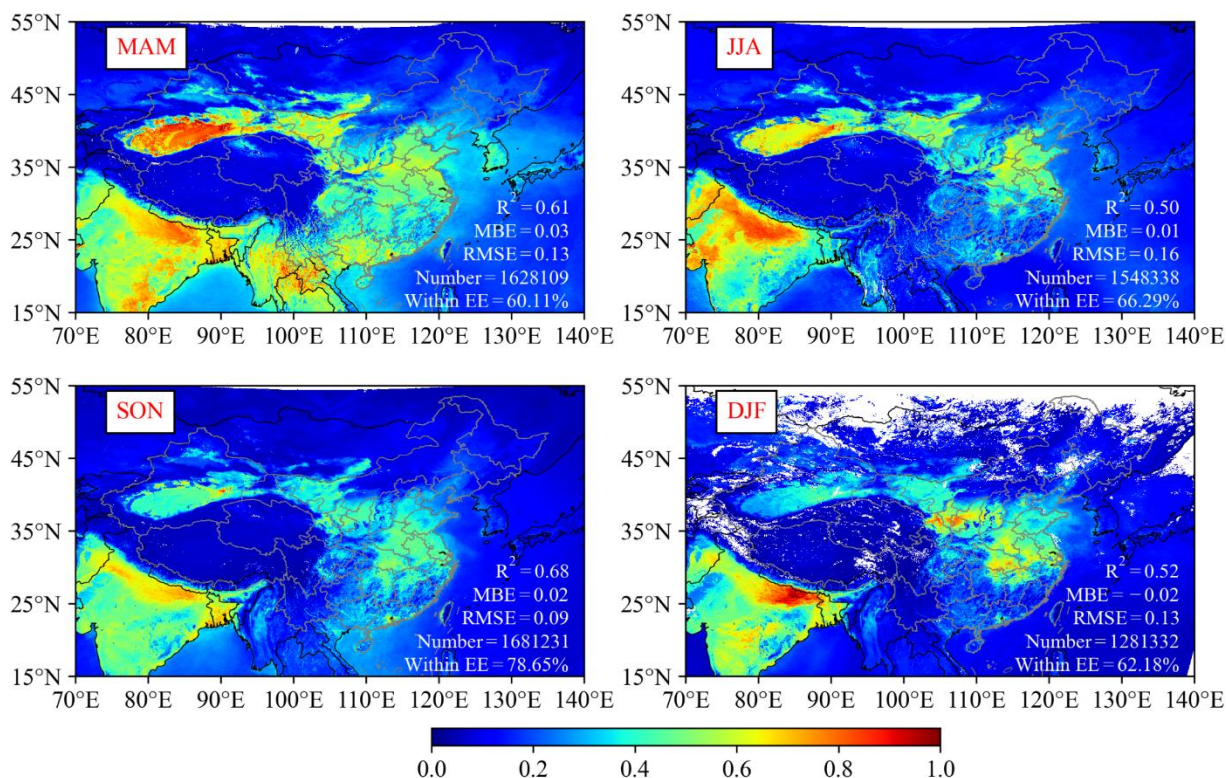
Fig. 7. Spatial distributions of seasonal mean AGRI AOD derived from the proposed hybrid algo-
rithm for the year 2018. The statistics (R^2, MBE, RMSE, Number, and Percentage within EE) in
the figure are calculated using the seasonal mean MAIAC AOD and AGRI AOD.

475

4.3 Extreme pollution event

An extreme aerosol case is selected here to demonstrate the advantages of AGRI AOD under
such situations, which can be frequent in various parts of Asia. As shown in Fig. 8, the air quality
at Beijing (one of the 9 testing stations) on the afternoon of November 1, 2018 significantly dete-
riorated compared to the morning: AOD increased from 0.09 at 00:50 to 0.52 at 07:45 (universal
time, 8 hours behind local time). However, MAIAC AOD provides limited information, as only
two AOD values are reported for that day (i.e., 0.19 at 02:30 and 0.24 at 05:30). Encouragingly,
AGRI AOD provides 33 observations for that day and reflects the continuous increase in AOD,
reaching a maximum value of 0.44 in the afternoon. Remarkably, the AGRI AOD remains within
±0.1 of the ground-truth observations. The overestimation in the early hours is likely associated
with the uncertainty in surface reflectance. As illustrated in Section 3.2, the surface reflectance

21

used in the present method is not strictly aerosol-free, Rayleigh- and gas-corrected. Hence, any underestimation in surface reflectance leads to an overestimation of AGRI AOD.

In Fig. 9, the AGRI AOD is overlayed with an RGB true-color image (also from AGRI) on November 1, 2018. The red rectangle covering the Beijing–Tianjin–Hebei area is the region of interest (ROI). At 01:30 UTC, only ~50% of the ROI had an AOD value exceeding 0.4, with high values being concentrated in the southwest. Over time, the area with AOD exceeding 0.4 within the ROI gradually increased and reached nearly 75% of the ROI at 07:30 UTC. This gradual development process is not reflected by MAIAC AOD because of its coarser temporal resolution. The three additional cases displayed in Fig. 10 also demonstrate the excellent results of the AGRI-based proposed method when applied to the monitoring of urban aerosols over areas where air pollution is variable and often significant, like in Beijing. The figure underlines that the present method can provide AOD retrievals that are comparable to the ground truth—and often better than those of MAIAC—under low-, medium-, or high-AOD situations.
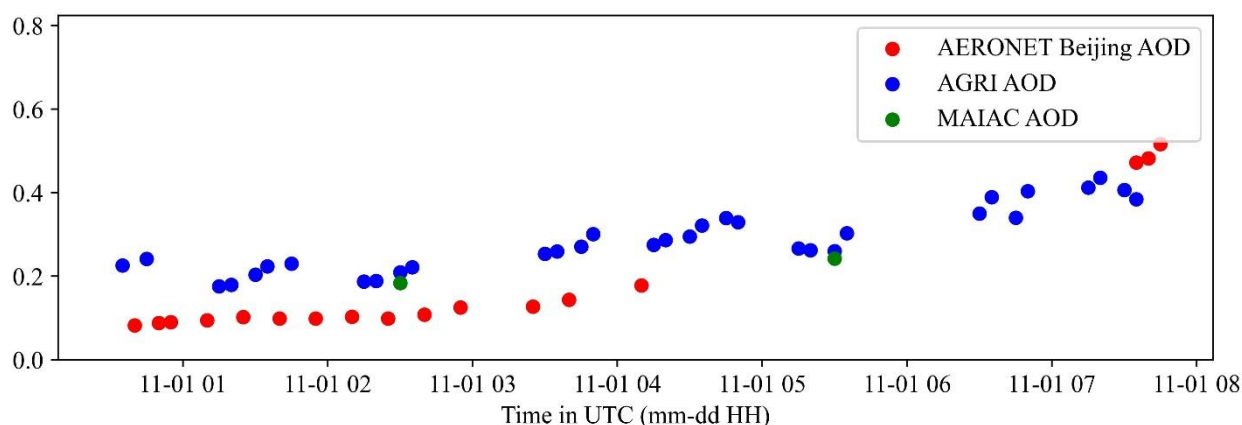
Fig 8. Variations of AERONET AOD (red), AGRI AOD (blue), and MAIAC AOD (green) at Beijing (116.38°E, 39.98°N) on November 1, 2018.
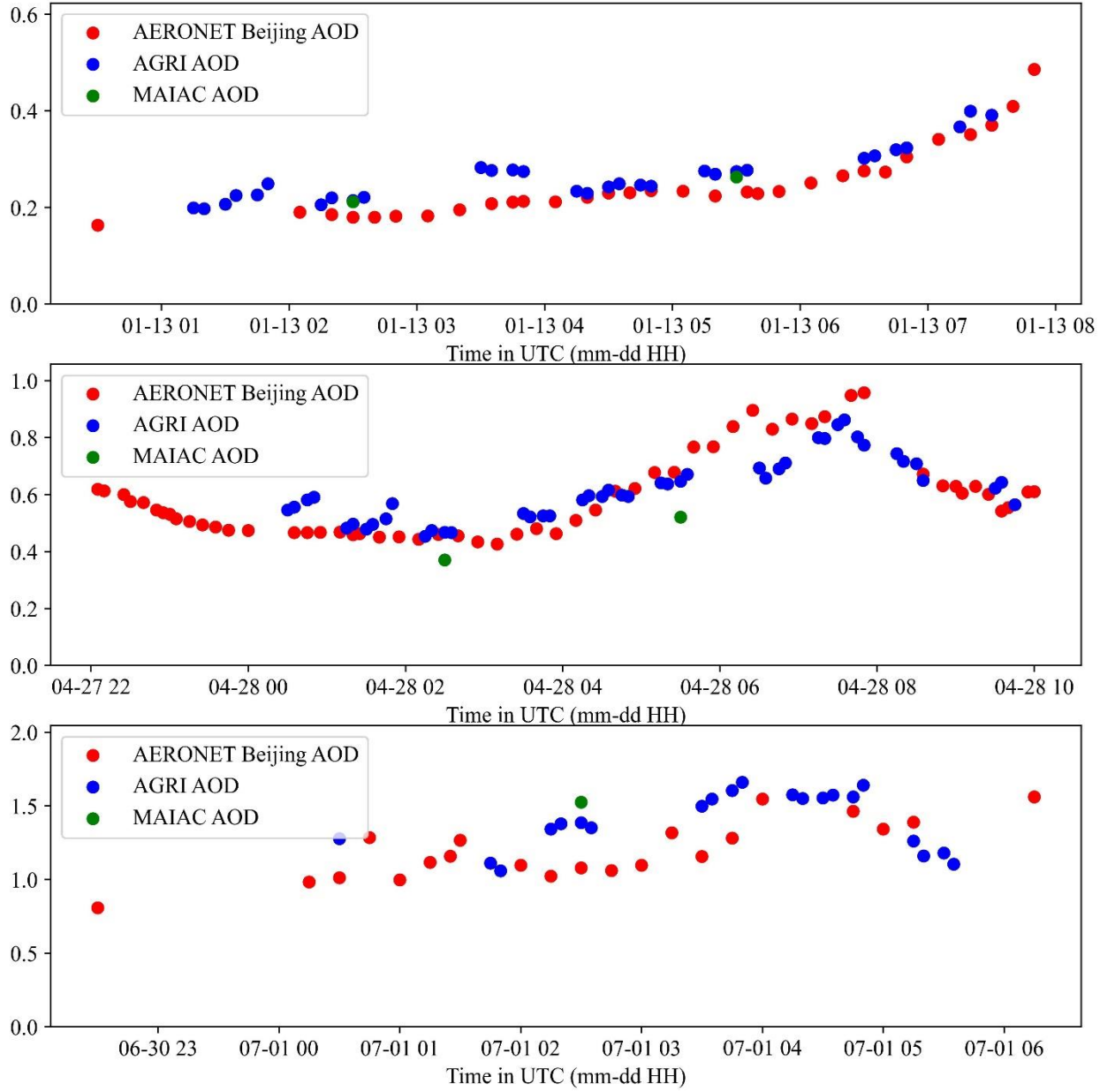
504

505
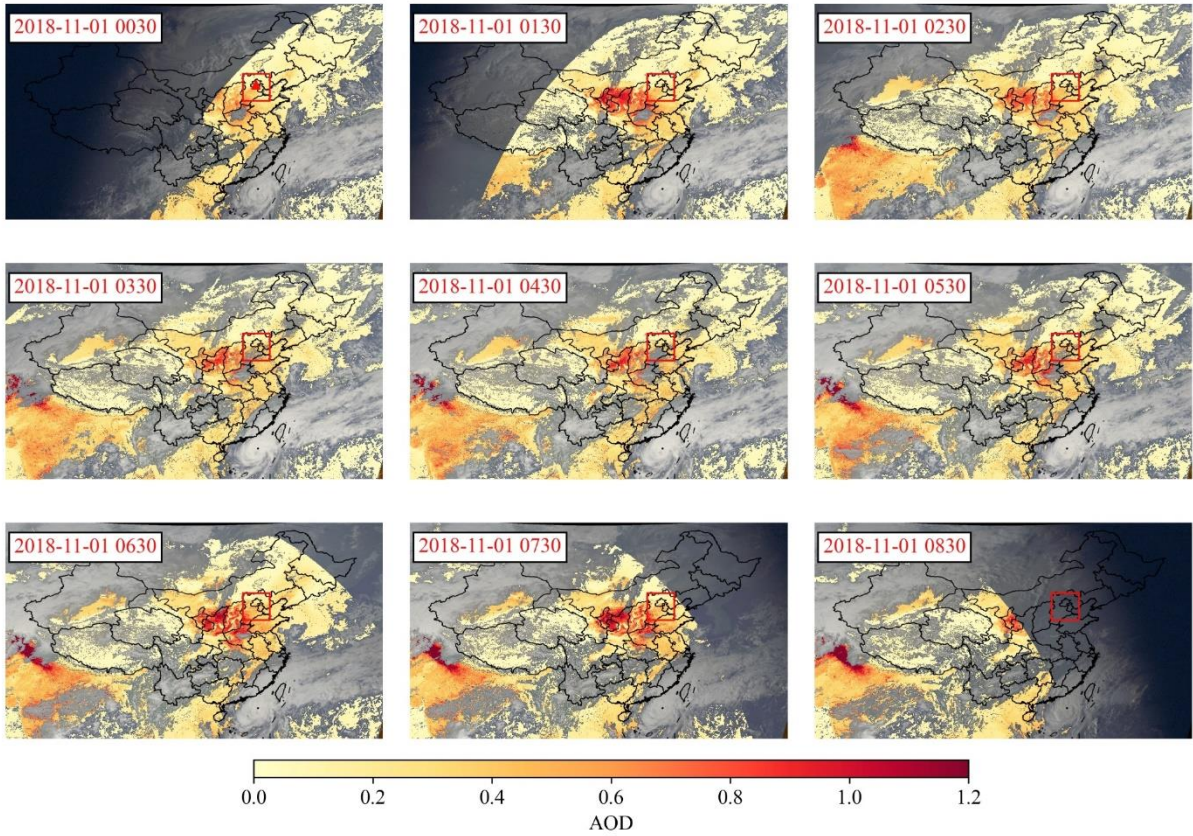
Fig. 9. Hourly FY-4A/AGRI AOD dataset from 00:30 UTC on November 1, 2018, to 08:30 UTC on November 1, 2018. The red triangle indicates the AERONET Beijing station and the red rectangle represents the Beijing-Tianjin-Hebei region.

Fig. 10. Variations of AERONET AOD (red), AGRI AOD (blue), and MAIAC AOD (green) at Beijing (116.38°E, 39.98°N) on January 13, 2018, April 28, 2018, and July 1, 2018 (from top to bottom).

4.4 Feature contribution and uncertainty analysis

The Shapley additive explanations (SHAP) method proposed by Lundberg and Lee [63] is used here for model interpretability. This method assigns a contribution to each prediction feature by considering the marginal contribution of the feature when it is present. Table 4 displays the contributions of the top-10 model features on AGRI AOD retrievals. It is evident from the results that ELV, R_{650}, R_{470}, and PWV are the four most important features (in terms of their absolute

magnitude). Remarkably, higher values of these features correspond to smaller values of AGRI AOD. A plausible explanation for this trend is that the high values of ELV are found over north-west China where AOD is relatively low. Regarding R_{650} and R_{470}, higher values in these two channels generally indicate less extinction of solar radiance by aerosols, thus indicating lower AOD values. Additionally, relatively high PWV is commonly observed over the ocean with extremely humid air wobbling north and south of the Equator [64]. In contrast, high AOD values are closely associated with human activities over the land. Therefore, the negative contribution of PWV in the model likely reflects the difference in the respective spatial distributions of AOD and PWV. In contrast with the above four features, ρ_{650} exhibits a positive contribution, meaning that higher ρ_{650} values are associated with larger AODs. This explains why high ρ_{650} and AODs always jointly appear over the Tarim Basin, as inferred from the surface reflectance in Fig. 3 and the seasonal mean AODs in Fig. 7.

Table 4. Feature contributions to the AGRI AOD retrieval (only the top 10 features are presented).

Feature Name	Contribution
ELV	−0.23
R_{650}	−0.14
R_{470}	−0.13
PWV	−0.12
ρ_{650}	0.08
CSZA	0.08
ρ_{2250}	−0.05
R_{2250}	0.04
MCD12C1	−0.04
ρ_{470}	0.02

Table 5. Sensitivity study for the input features of AGRI AOD retrievals.

Input feature	Benchmark input value[*]	Assumed relative uncertainty in input[**] (%)	Range of relative error in AOD retrieval (%)
R_{650}	0.09	±5%	[−18.88%, 10.43%]
R_{470}	0.11	±5%	[−17.23%, 14.01%]
PWV	9.39	±5%	[−4.21%, 4.07%]
ρ_{650}	0.09	±9%	[11.74%, -10.80%]

[*] The benchmark of stimulation is extracted from the input features at the AERONET Beijing site on November 1, 2018. Specifically, R_{650} and R_{470} are the TOA reflectances from AGRI; PWV is derived from ERA5; ρ_{650} is the surface reflectance proxy at 650 nm.

543   According to the order of feature contributions in Table 4, sensitivity experiments are con-

544   ducted for the top features. ELV is excluded here because of its high accuracy [66]. Therefore,

545   only R_{650}, R_{470}, PWV, and ρ_{650} are selected for this sensitivity study. These specific variables are

546   of obvious interest because the errors in sensors, reanalysis, and the surface reflectance proxy are

547   expected to propagate down to the AOD retrieval. Table 5 summaries the sensitivity of the re-

548   trieved AOD for these features. As shown in the table, the largest error sources are R_{650} and R_{470},

549   whose relative errors in AOD retrievals vary from –18.88% to 10.43% and –17.23% to 14.01%,

550   respectively. The somewhat related surface reflectance at 650 nm (ρ_{650}) is the third largest source

551   of error, as a consequence of the large relative uncertainty in ρ_{650} ($\pm 9\%$).

5. Conclusion

554   In this study, the AOD over land and ocean is estimated using a deep-learning and transfer-

555   learning hybrid aerosol retrieval algorithm based on the AGRI sensor onboard the FY-4A geosta-

556   tionary satellite. This specific retrieval approach has been followed because a DNN requires large

557   datasets to train network models, whereas the number of ground-based sunphotometer stations is

558   limited.

559   The proposed algorithm first uses 10-min AHI AODs as targets to train a baseline model (DNN

560   with skip connections). Another core part of the hybrid algorithm is based on transfer learning,

561   which, on top of the baseline model, uses sunphotometer AOD observations from 89 ground sta-

562   tions to fine-tune the parameters of the fully connected layer. The proposed algorithm ensures that

563   sufficient samples exist to efficiently train the baseline model and that the subsequent fine-tuning

564   results in sufficient portability over the whole domain.

565   The algorithm was applied to a one-year AGRI dataset for evaluation. Compared with the

566   baseline model, employing transfer learning for fine-tuning has been shown to substantially im-

567   prove the model performance. The R^2 increased from 0.63 to 0.70, while the RMSE and MBE

568   decreased from 0.19 and 0.06 to 0.15 and 0.03, respectively. Moreover, 70.7% of the results were

found within the EE, i.e., a ~20% improvement over the baseline value of 51.3%. In applications where AOD is needed to study extreme aerosol events, the present 5-min AGRI retrievals offer the important advantage of providing multiple AOD estimates during the day, at least in the absence of clouds over 4-km pixels. The Feature Importance study showed that the top-5 features contributing to the AOD retrieval are ELV, R_{650}, R_{470}, PWV, and ρ_{650}. Considering the uncertainties and impacts of input features, R_{650}, R_{470} and ρ_{650} were found the three largest error sources in the retrievals, followed by PWV. This study has demonstrated the great potential of combining the physical approach and deep learning in geoscientific analysis. The proposed algorithm can also be applied to other multi-spectral sensors, such as AGRI on FY-4B.

Nevertheless, the present algorithm has still room for improvement. For example, the cloud detection method can affect the estimation of surface reflectance as well as the coverage of the retrieved AGRI AOD. More generally, the accuracy of aerosol retrieval techniques is closely tied to exclude unsuitable pixels. Failure to accurately identify polluted layers as clouds or misclassifying clouds as polluted layers can lead to erroneous AOD estimates. These errors not only affect the overall quality of AOD products but also hinder the interpretation and utilization of remote sensing data for various applications. Therefore, improvements to the cloud mask are being envisioned to improve the accuracy of the AGRI AOD in the future. Any other improvement in the determination of the surface reflectance at 650 nm would also be useful. If the proposed method is intended to be implemented operationally, the present reliance on the ERA5 reanalysis to obtain the input features poses a challenge because of its significant time delay. A possible alternative would be to rather obtain such data from a nowcast or forecast datastream provided by institutions such as CMA, ECMWF, or NOAA.

Moreover, the present method employed AHI AOD as an intermediate target for the model. However, directly extracting its direct impact on AGRI AOD is not a viable approach. To evaluate this impact, future investigations should consider utilizing two different versions of AHI AOD datasets. Furthermore, the present analysis focused on east Asia, where many sunphotometer stations exist. Further studies are needed to expand the validation to the whole FY-4A domain, i.e., including other regions of Asia, Australia, and the oceans.

Data availability

The ERA5 data can be found at https://cds.climate.copernicus.eu/#!/home. The MODIS data can be found at https://www.earthdata.nasa.gov/. The AHI AOD data is available at http://www.eorc.jaxa.jp/ptree/index.html. The AERONET data can be accessed from https://aeronet.gsfc.nasa.gov/. CARSNET data can be obtained on request from Professor Huizheng Che (chehz@cma.gov.cn). The FY-4A datasets are obtained from http://data.nsmc.org.cn. The retrieved AGRI AOD can be requested by contacting Disong Fu (fudisong@mail.iap.ac.cn).

References

[1]   IPCC. IPCC Sixth Assessment Report - Climate Change 2021: The Physical Science Basis. Chapter 7: The Earth's Energy Budget, Climate Feedbacks and Climate Sensitivity. 2021. https://doi.org/10.1017/9781009157896.009.923.

[2]   Seinfeld JH, Bretherton C, Carslaw KS, Coe H, DeMott PJ, Dunlea EJ, et al. Improving our fundamental understanding of the role of aerosol-cloud interactions in the climate system.   Proc   Natl   Acad   Sci   U   S   A   2016;113:5781–90. https://doi.org/10.1073/pnas.1514043113.

[3]   Chudnovsky AA, Koutrakis P, Kloog I, Melly S, Nordio F, Lyapustin A, et al. Fine particulate matter predictions using high resolution Aerosol Optical Depth (AOD) retrievals.   Atmos   Environ   2014;89:189–98. https://doi.org/10.1016/j.atmosenv.2014.02.019.

[4]   Butt EW, Rap A, Schmidt A, Scott CE, Pringle KJ, Reddington CL, et al. The impact of residential combustion emissions on atmospheric aerosol, human health, and climate. Atmos Chem Phys 2016;16:873–905. https://doi.org/10.5194/acp-16-873-2016.

[5]   Bréon FM, Vermeulen A, Descloitres J. An evaluation of satellite aerosol products against sunphotometer   measurements.   Remote   Sens   Environ   2011;115:3102–11. https://doi.org/10.1016/j.rse.2011.06.017.

[6]   de Leeuw G, Holzer-Popp T, Bevan S, Davies WH, Descloitres J, Grainger RG, et al.

Evaluation of seven European aerosol optical depth retrieval algorithms for climate analysis. Remote Sens Environ 2015;162:295–315. https://doi.org/10.1016/j.rse.2013.04.023.

[7] Mhawish A, Sorek-Hamer M, Chatfield R, Banerjee T, Bilal M, Kumar M, et al. Aerosol characteristics from earth observation systems: A comprehensive investigation over South Asia (2000–2019). Remote Sens Environ 2021;259:112410. https://doi.org/10.1016/j.rse.2021.112410.

[8] Xia X, Che H, Shi H, Chen H, Zhang X, Wang P, et al. Advances in sunphotometer-measured aerosol optical properties and related topics in China: Impetus and perspectives. Atmos Res 2021;249:105286. https://doi.org/10.1016/j.atmosres.2020.105286.

[9] Gueymard CA, Yang D. Worldwide validation of CAMS and MERRA-2 reanalysis aerosol optical depth products using 15 years of AERONET observations. Atmos Environ 2020;225:117216. https://doi.org/10.1016/j.atmosenv.2019.117216.

[10] Holben BN, Eck TF, Slutsker I, Tanré D, Buis JP, Setzer A, et al. AERONET - A federated instrument network and data archive for aerosol characterization. Remote Sens Environ 1998;66:1–16. https://doi.org/10.1016/S0034-4257(98)00031-5.

[11] Giles DM, Sinyuk A, Sorokin MG, Schafer JS, Smirnov A, Slutsker I, et al. Advancements in the Aerosol Robotic Network (AERONET) Version 3 database - Automated near-real-time quality control algorithm with improved cloud screening for Sun photometer aerosol optical depth (AOD) measurements. Atmos Meas Tech 2019;12:169–209. https://doi.org/10.5194/amt-12-169-2019.

[12] Nakajima T, Campanelli M, Che H, Estellés V, Irie H, Kim SW, et al. An overview of and issues with sky radiometer technology and SKYNET. Atmos Meas Tech 2020;13:4195–218. https://doi.org/10.5194/amt-13-4195-2020.

[13] Che H, Xia X, Zhao H, Dubovik O, Holben BN, Goloub P, et al. Spatial distribution of aerosol microphysical and optical properties and direct radiative effect from the China Aerosol Remote Sensing Network. Atmos Chem Phys 2019;19:11843–64. https://doi.org/10.5194/acp-19-11843-2019.

[14] Xin J, Wang YY, Pan Y, Ji D, Liu Z, Wen T, et al. The campaign on atmospheric aerosol research network of China: CARE-China. Bull Am Meteorol Soc 2015;96:1137–55. https://doi.org/10.1175/BAMS-D-14-00039.1.

[15] Li ZQ, Xu H, Li KT, Li DH, Xie YS, Li L, et al. Comprehensive Study of Optical, Physical, Chemical, and Radiative Properties of Total Columnar Atmospheric Aerosols over China: An Overview of Sun–Sky Radiometer Observation Network (SONET) Measurements. Bull Am Meteorol Soc 2018;99:739–55. https://doi.org/10.1175/BAMS-D-17-0133.1.

[16] Schmetz J, Pili P, Tjemkes S, Just D, Kerkmann J, Rota S, et al. An introduction to Meteosat Second Generation (MSG). Bull Am Meteorol Soc 2002;83:977–92. https://doi.org/10.1175/1520-0477(2002)083<0977:AITMSG>2.3.CO;2.

[17] Bessho K, Date K, Hayashi M, Ikeda A, Imai T, Inoue H, et al. An introduction to Himawari-8/9 — Japan's new-generation geostationary meteorological satellites. J Meteorol Soc Japan 2016;94:151–83. https://doi.org/10.2151/jmsj.2016-009.

[18] Choi H, Park S, Kang Y, Im J, Song S. Retrieval of hourly PM2.5 using top-of-atmosphere reflectance from geostationary ocean color imagers I and II. Environ Pollut 2023;323:121169. https://doi.org/10.1016/j.envpol.2023.121169.

[19] Yang J, Zhang Z, Wei C, Lu F, Guo Q. Introducing the New Generation of Chinese

678   Geostationary Weather Satellites, Fengyun-4. Bull Am Meteorol Soc 2017;98:1637–58.
679   https://doi.org/10.1175/BAMS-D-16-0065.1.

680 [20] Zhang P, Zhu L, Tang S, Gao L, Chen L, Zheng W, et al. General comparison of FY-
681   4A/AGRI with other GEO/LEO instruments and its potential and challenges in non-
682   meteorological   applications.   Front   Earth   Sci   2019;6:1–13.
683   https://doi.org/10.3389/feart.2018.00224.

684 [21] Kaufman YJ, Tanré D, Remer LA, Vermote EF, Chu A, Holben BN. Operational remote
685   sensing of tropospheric aerosol over land from EOS moderate resolution imaging
686   spectroradiometer.   J   Geophys   Res   Atmos   1997;102:17051–67.
687   https://doi.org/10.1029/96jd03988.

688 [22] Hsu NC, Tsay SC, King MD, Herman JR. Aerosol properties over bright-reflecting source
689   regions.   IEEE   Trans   Geosci   Remote   Sens   2004;42:557–69.
690   https://doi.org/10.1109/TGRS.2004.824067.

691 [23] Hsu NC, Jeong MJ, Bettenhausen C, Sayer AM, Hansell R, Seftor CS, et al. Enhanced Deep
692   Blue aerosol retrieval algorithm: The second generation. J Geophys Res Atmos
693   2013;118:9296–315. https://doi.org/10.1002/jgrd.50712.

694 [24] Hsu NCC, Lee J, Sayer AMM, Carletta N, Chen SHH, Tucker CJJ, et al. Retrieving near-
695   global aerosol loading over land and ocean from AVHRR. J Geophys Res Atmos
696   2017;122:9968–89. https://doi.org/10.1002/2017JD026932.

697 [25] Lyapustin A, Wang Y, Laszlo I, Kahn R, Korkin S, Remer L, et al. Multiangle
698   implementation of atmospheric correction (MAIAC): 2. Aerosol algorithm. J Geophys Res
699   Atmos 2011;116:1–15. https://doi.org/10.1029/2010JD014986.

700 [26] Dubovik O, Lapyonok T, Litvinov P, Herman M, Fuertes D, Ducos F, et al. GRASP: a
701   versatile algorithm for characterizing the atmosphere. SPIE Newsroom 2014.
702   https://doi.org/10.1117/2.1201408.005558.

703 [27] ATBD AA. GOES-R Advanced Baseline Imager (ABI) Algorithm Theoretical Basis
704   Document For Suspended Matter/Aerosol Optical Depth and Aerosol Size Parameter.
705   NOAA/NESDIS/STAR 2018:1–60.

706 [28] Yoshida M, Kikuchi M, Nagao TM, Murakami H, Nomaki T, Higurashi A. Common
707   retrieval of aerosol properties for imaging satellite sensors. vol. 96B. 2018.
708   https://doi.org/10.2151/JMSJ.2018-039.

709 [29] She L, Zhang HK, Li Z, de Leeuw G, Huang B. Himawari-8 Aerosol Optical Depth (AOD)
710   Retrieval Using a Deep Neural Network Trained Using AERONET Observations. Remote
711   Sens 2020;12:4125. https://doi.org/10.3390/rs12244125.

712 [30] Yeom J-MM, Jeong S, Ha J-SS, Lee K-HH, Lee C-SS, Park S. Estimation of the Hourly
713   Aerosol Optical Depth From GOCI Geostationary Satellite Data: Deep Neural Network,
714   Machine Learning, and Physical Models. IEEE Trans Geosci Remote Sens 2022;60:1–12.
715   https://doi.org/10.1109/TGRS.2021.3107542.

716 [31] Kang Y, Kim M, Kang E, Cho D, Im J. Improved retrievals of aerosol optical depth and
717   fine mode fraction from GOCI geostationary satellite data using machine learning over East
718   Asia.   ISPRS   J   Photogramm   Remote   Sens   2022;183:253–68.
719   https://doi.org/10.1016/j.isprsjprs.2021.11.016.

720 [32] Chen X, Leeuw G De. Joint retrieval of the aerosol fine mode fraction and optical depth
721   using MODIS spectral reflectance over northern and eastern China : Artificial neural

722   network method. Remote Sens Environ 2020;249:112006. https://doi.org/10.1016/j.rse.2020.112006.

724 [33] Jiang X, Xue Y, Jin C, Bai R, Sun Y, Wu S. A Simple Band Ratio Library (BRL) Algorithm for Retrieval of Hourly Aerosol Optical Depth Using FY-4A AGRI Geostationary Satellite Data. Remote Sens 2022;14. https://doi.org/10.3390/rs14194861.

727 [34] Xie Y, Li Z, Guang J, Hou W, Salam A, Ali Z, et al. Aerosol Optical Depth Retrieval over South Asia Using FY-4A/AGRI Data. IEEE Trans Geosci Remote Sens 2022;60:1. https://doi.org/10.1109/TGRS.2021.3124421.

730 [35] Ding H, Zhao L, Liu S, Chen X, de Leeuw G, Wang F, et al. FY-4A/AGRI Aerosol Optical Depth Retrieval Capability Test and Validation Based on NNAeroG. Remote Sens 2022;14:5591. https://doi.org/10.3390/rs14215591.

733 [36] Min M, Wu C, Li C, Liu H, Xu N, Wu X, et al. Developing the science product algorithm testbed for Chinese next-generation geostationary meteorological satellites: Fengyun-4 series. J Meteorol Res 2017;31:708–19. https://doi.org/10.1007/s13351-017-6161-z.

736 [37] Cox C, Munk W. Measurement of the Roughness of the Sea Surface from Photographs of the Sun's Glitter. J Opt Soc Am 1954;44:838. https://doi.org/10.1364/JOSA.44.000838.

738 [38] Hersbach H, Bell B, Berrisford P, Hirahara S, Horányi A, Muñoz-Sabater J, et al. The ERA5 global reanalysis. Q J R Meteorol Soc 2020;146:1999–2049. https://doi.org/10.1002/qj.3803.

741 [39] Fu D, Gueymard CA, Yang D, Zheng Y, Xia X, Bian J. Improving aerosol optical depth retrievals from Himawari-8 with ensemble learning enhancement: Validation over Asia. Atmos Res 2023;284:106624. https://doi.org/10.1016/j.atmosres.2023.106624.

744 [40] Sulla-Menashe D, Friedl MA. User Guide to Collection 6 MODIS Land Cover Dynamics (MCD12Q2) Product. USGS 2018;6:1–8.

746 [41] Bilal M, Nichol JE, Bleiweiss MP, Dubois D. A Simplified high resolution MODIS aerosol retrieval algorithm (SARA) for use over mixed surfaces. Remote Sens Environ 2013;136:135–45. https://doi.org/10.1016/j.rse.2013.04.014.

749 [42] Su X, Wang L, Zhang M, Qin W, Bilal M. A High-Precision Aerosol Retrieval Algorithm (HiPARA) for Advanced Himawari Imager (AHI) data: Development and verification. Remote Sens Environ 2021;253:112221. https://doi.org/10.1016/j.rse.2020.112221.

752 [43] Chen Y, Fan M, Li M, Li Z, Tao J, Wang Z, et al. Himawari-8/AHI Aerosol Optical Depth Detection Based on Machine Learning Algorithm. Remote Sens 2022;14. https://doi.org/10.3390/rs14132967.

755 [44] Hu Y, Liu L, Liu L, Peng D, Jiao Q, Zhang H. A landsat-5 atmospheric correction based on MODIS atmosphere products and 6s model. IEEE J Sel Top Appl Earth Obs Remote Sens 2014;7:1609–15. https://doi.org/10.1109/JSTARS.2013.2290028.

758 [45] Lecun Y, Bengio Y, Hinton G. Deep learning. Nature 2015;521:436–44. https://doi.org/10.1038/nature14539.

760 [46] He K, Zhang X, Ren S, Sun J. Deep residual learning for image recognition. Proc IEEE Comput Soc Conf Comput Vis Pattern Recognit 2016;2016-Decem:770–8. https://doi.org/10.1109/CVPR.2016.90.

763 [47] Weng W, Zhu X. U-Net: Convolutional Networks for Biomedical Image Segmentation. IEEE Access 2021;9:16591–603. https://doi.org/10.1109/ACCESS.2021.3053408.

765 [48] Drozdzal M, Vorontsov E, Chartrand G, Kadoury S, Pal C. The importance of skip

connections in biomedical image segmentation. Lect Notes Comput Sci (Including Subser Lect Notes Artif Intell Lect Notes Bioinformatics) 2016;10008 LNCS:179–87. https://doi.org/10.1007/978-3-319-46976-8_19.

[49]   Kingma DP, Ba JL. Adam: A method for stochastic optimization. 3rd Int Conf Learn Represent ICLR 2015 - Conf Track Proc 2015:1–15.

[50]   Ren J, Zhang M, Yu C, Liu Z. Balanced MSE for Imbalanced Visual Regression. Proc IEEE Comput Soc Conf Comput Vis Pattern Recognit 2022;2022-June:7916–25. https://doi.org/10.1109/CVPR52688.2022.00777.

[51]   Steininger M, Kobs K, Davidson P, Krause A, Hotho A. Density-based weighting for imbalanced regression. Mach Learn 2021;110:2187–211. https://doi.org/10.1007/s10994-021-06023-5.

[52]   Tan Y, Wang Q, Zhang Z. Assessing spatiotemporal variations of AOD in Japan based on Himawari-8 L3 V31 aerosol products: Validations and applications. Atmos Pollut Res 2022;13:101439. https://doi.org/10.1016/j.apr.2022.101439.

[53]   Feng L, Su X, Wang L, Jiang T, Zhang M, Wu J, et al. Accuracy and error cause analysis, and recommendations for usage of Himawari-8 aerosol products over Asia and Oceania. Sci Total Environ 2021;796:148958. https://doi.org/10.1016/j.scitotenv.2021.148958.

[54]   Yosinski J, Clune J, Bengio Y, Lipson H. How transferable are features in deep neural networks? Adv Neural Inf Process Syst 2014;4:3320–8.

[55]   Liu Z, Yang Q, Shao J, Wang G, Liu H, Tang X, et al. Improving daily precipitation estimation in the data scarce area by merging rain gauge and TRMM data with a transfer learning framework. J Hydrol 2022;613:128455. https://doi.org/10.1016/j.jhydrol.2022.128455.

[56]   Sayer AM, Munchak LA, Hsu NC, Levy RC, Bettenhausen C, Jeong M-J. MODIS Collection 6 aerosol products: Comparison between Aqua's e-Deep Blue, Dark Target, and "merged" data sets, and usage recommendations. J Geophys Res Atmos 2014;119:13,965-13,989. https://doi.org/10.1002/2014JD022453.

[57]   Levy RC, Mattoo S, Munchak LA, Remer LA, Sayer AM, Patadia F, et al. The Collection 6 MODIS aerosol products over land and ocean. Atmos Meas Tech 2013;6:2989–3034. https://doi.org/10.5194/amt-6-2989-2013.

[58]   Jiang X, Xue Y, Jin C, Bai R, Li N, Sun Y. Retrieval of Aerosol Optical Depth Over Land Using Fy-4Aagri Geostationary Satellite Data. 2021 IEEE Int. Geosci. Remote Sens. Symp. IGARSS, IEEE; 2021, p. 1931–4. https://doi.org/10.1109/IGARSS47720.2021.9554807.

[59]   Song Z, Fu D, Zhang X, Wu Y, Xia X, He J, et al. Diurnal and seasonal variability of PM2.5 and AOD in North China plain: Comparison of MERRA-2 products and ground measurements. Atmos Environ 2018;191:70–8. https://doi.org/10.1016/j.atmosenv.2018.08.012.

[60]   Wang P, Tang Q, Zhu Y, Zheng K, Liang T, Yu Q, et al. Validation and Analysis of MAIAC AOD Aerosol Products in East Asia from 2011 to 2020. Remote Sens 2022;14:5735. https://doi.org/10.3390/rs14225735.

[61]   Mhawish A, Banerjee T, Sorek-Hamer M, Lyapustin A, Broday DM, Chatfield R. Comparison and evaluation of MODIS Multi-angle Implementation of Atmospheric Correction (MAIAC) aerosol product over South Asia. Remote Sens Environ 2019;224:12–28. https://doi.org/10.1016/j.rse.2019.01.033.

[62] Qin W, Fang H, Wang L, Wei J, Zhang M, Su X, et al. MODIS high-resolution MAIAC aerosol product: Global validation and analysis. Atmos Environ 2021;264:118684. https://doi.org/10.1016/j.atmosenv.2021.118684.

[63] Lundberg SM, Lee SI. A unified approach to interpreting model predictions. Adv. Neural Inf. Process. Syst., vol. 2017- Decem, 2017, p. 4766–75.

[64] Chen B, Liu Z. Global water vapor variability and trend from the latest 36 year (1979 to 2014) data of ECMWF and NCEP reanalyses, radiosonde, GPS, and microwave satellite. J Geophys Res Atmos 2016;121:238. https://doi.org/10.1002/2016JD024917.

[65] Wang S, Xu T, Nie W, Jiang C, Yang Y, Fang Z, et al. Evaluation of precipitablewater vapor from five reanalysis products with ground-based GNSS observations. Remote Sens 2020;12. https://doi.org/10.3390/rs12111817.

[66] Ibrahim M, Al-Mashaqbah A, Koch B, Datta P. An evaluation of available digital elevation models (DEMs) for geomorphological feature analysis. Environ Earth Sci 2020;79:1–11. https://doi.org/10.1007/s12665-020-09075-3.